

BoltzmaNN: Deriving effective pair potentials and equations of state using neural networks

Fabian Berressem,¹ Mihir R. Khadilkar,¹ and Arash Nikoubashman^{1, a)}

Institute of Physics, Johannes Gutenberg University Mainz, Staudingerweg 7, 55128 Mainz, Germany

(Dated: August 8, 2019)

In this work we investigate the use of neural networks (NNs) to devise effective equations of state from a given isotropic pair potential using the virial expansion of the pressure. We train the NNs with data from molecular dynamics simulations, sampled in the NVT ensemble at densities covering both the gas- and liquid-like regime. We find that the NNs provide much more accurate results compared to the analytic estimate of the second virial coefficient derived in the low density limit. Further, we design and train NNs for computing the potential of mean force from the radial pair distribution function, $g(r)$, a task which is often performed for inverse design and coarse-graining applications. Here, we find that a good choice for the loss function is crucial for an accurate prediction of the pair potentials. In both use cases, we study in detail how providing additional information about forces and the density impacts the performance of the NNs. We find that including this additional information greatly increases the quality of the predictions, since more correlations are taken into account; the predicted potentials become smoother and are in general significantly closer to the real potential as well as more transferable.

I. INTRODUCTION

Understanding and predicting the relationship between the (macroscopic) properties of a material and its (microscopic) building blocks is one of the key challenges in materials research and physics. One important goal in statistical physics is the accurate prediction of the phase behavior on the basis of the (effective) pair potential $U(r)$. According to van der Waals' theorem of corresponding states, all simple fluids obey the same reduced equation of state (EOS), if the thermodynamic variables are rescaled by their value at the critical point. However, this law only applies for systems with conformal pair potentials, *i.e.* when the potentials can be fully superimposed by adjusting the interaction strength, ϵ , and particle diameter, σ , which is rarely the case in practice. Noro and Frenkel extended this principle by including in the prediction the reduced second virial coefficient for quantifying the effective range of the attraction.¹ This extended approach provides accurate predictions for pair potentials which are characterized by attractive interactions whose ranges are much smaller than the particle size,^{1,2} but it is expected to fail for more complex pair potentials which, *e.g.*, include a repulsive barrier. Since a large number of (effective) pair potentials in soft matter are bounded or have repulsive barriers,³⁻⁷ alternative prediction tools are highly desirable.

Progress in this field has wide implications, not just in terms of fundamental understanding, but also due to the large number of potential technological applications. Various mechanical, optical, and electronic properties of materials critically depend on the degree of ordering of their atomic or (macro)molecular constituents.

These properties include photonic band gaps,⁸ thermal coefficients,⁹ as well as porosity.¹⁰ In the conventional *forward design* approach, the development of novel materials typically begins with designing candidate building blocks that are expected to lead to the desired functional properties. Then these candidates are created, tested for viability, and, if necessary, modified, until the compound with the desired properties has been identified. It is clear that this iterative procedure requires much experience, since a bad initial candidate can dramatically slow down the convergence. Due to these inherent issues, there has been a recent paradigm shift towards the *inverse design* process, where the target properties are given and the task is to find building blocks that lead to the desired output. In recent years, tuning the inter-particle interactions to design and control structural properties has been explored for a range of soft materials, including athermal granular media,¹¹ colloids,^{12,13} and block copolymers.^{14,15}

A number of techniques has been developed in the past for this inverse design process, including Reverse Monte Carlo (RMC) techniques,¹⁶⁻¹⁸ Iterative Boltzmann Inversion (IBI),¹⁹ simulated annealing-based optimization,²⁰ or Relative Entropy Minimization.²¹ In recent years, informatics-driven approaches have gained popularity that utilize machine learning (ML) algorithms on large databases to identify previously unrecognized patterns and to predict new candidate materials.²²⁻²⁷ In this work, we followed this heuristic approach, and employ artificial neural networks (NNs) for developing effective EOS from a given isotropic pair potential $U(r)$ using the virial expansion of the pressure. Further, we design and train NNs for computing the potential of mean force (PMF) from a given radial pair distribution function, $g(r)$. The training and test data for the NNs are generated from Molecular Dynamics (MD) simulations, performed in the canonical ensemble at densities covering both the gas-

^{a)}Electronic mail: anikouba@uni-mainz.de

and liquid-like regime.

The rest of this manuscript is organized as follows. In Section II, we provide a brief summary of the theoretical background, and explain the numerical methodologies we used. In Section III, we report the results from our inverse design process, where Section III A focuses on using NNs for determining the EOS via an effective second virial coefficient. In Section III B, we design and train NNs for computing the PMF from the radial pair distribution function. Section IV contains our conclusions and a brief outlook.

II. METHODOLOGY

A. Theoretical background

1. Effective equation of state

In order to describe the properties of a system, it is useful to deploy an EOS, which relates different state variables of the system under a given set of physical conditions. The EOS further allows to identify phase transitions of the system. For an ideal gas, the EOS reads

$$\mathcal{Z} := \frac{PV}{Nk_B T} = 1, \quad (1)$$

where \mathcal{Z} is the compressibility factor, P is the pressure, V is the volume, N is the number of particles, T is the temperature, and k_B is Boltzmann's constant. With $\beta \equiv 1/(k_B T)$ and $\rho \equiv N/V$, one can simplify Eq. (1) to $\mathcal{Z} = \beta P/\rho$. For a real gas, \mathcal{Z} differs from unity, and can be considered as a correction factor for the ideal gas law. One typically used extension of the ideal gas law to real gases is an expansion in terms of the density, which yields the virial expansion

$$\frac{\beta P}{\rho} = 1 + \sum_{i=2}^{\infty} B_i(T) \rho^{i-1} \quad (2)$$

with virial coefficients $B_i(T)$. Given below are, for example, the analytical expressions for the second and the third virial coefficient of a homogeneous fluid²⁸

$$B_2(T) = -\frac{1}{2} \int_V f(r, T) \, d\mathbf{r} \quad (3)$$

$$B_3(T) = -\frac{1}{3} \int_V \int_V f(r, T) f(r', T) f(|\mathbf{r} - \mathbf{r}'|, T) \, d\mathbf{r} d\mathbf{r}' \quad (4)$$

with the Mayer f -functions

$$f(r, T) = \exp[-\beta U(r)] - 1 \quad (5)$$

As one can see from Eq. (3), the second virial coefficient B_2 depends only on the pair interaction between the particles, while the third coefficient B_3 depends on two- and non-additive three-body interactions. In principle,

these coefficients can be derived from the grand canonical partition function or from diagrammatic methods in the canonical ensemble. In practice, however, it is usually not possible to determine these coefficients analytically, due to the complex nature of the underlying correlations. In the low-density limit, the EOS is dominated by pairwise terms so that the sum in Eq. (2) can be truncated at $i = 2$. In isotropic systems, one can solve the integral in Eq. (3) in polar coordinates, yielding

$$B_2(T) \approx -2\pi \int_0^{\infty} f(r, T) r^2 \, dr. \quad (6)$$

Thus, the EOS reads

$$\frac{\beta P}{\rho} \approx 1 - 2\pi\rho \int_0^{\infty} f(r, T) r^2 \, dr. \quad (7)$$

The approximative expression for the EOS given by Eq. (7) is rather useful, because it requires only knowledge about the pair potential $U(r)$, which is typically one of the input parameters in computer simulations. However, one should note that this result has been derived under the assumption of $\rho \rightarrow 0$, and thus it is questionable whether this expression can be utilized for predicting phase transitions, which typically occur at finite densities and involve also higher order correlations.

To address these shortcomings, one can introduce an effective second virial coefficient, $B_2^*(T, \rho)$, which implicitly contains the higher order terms of the virial expansion in the form of an explicit density dependence. With this quantity, the EOS can be written as

$$\frac{\beta P}{\rho} \approx 1 + \rho B_2^*(T, \rho). \quad (8)$$

This term cannot be computed analytically anymore, but it can be readily extracted from computer simulations in the canonical ensemble by measuring the pressure P at various temperatures, T , and densities, ρ . In this work, we apply NNs for the task of predicting $B_2^*(T, \rho)$ for a given pair potential. Hence, the NN should learn the mapping

$$U(r) \mapsto B_2^* := \frac{\mathcal{Z} - 1}{\rho} = \frac{\beta P - \rho}{\rho^2} \quad (9)$$

2. Potential prediction from pair distribution function

One important realization in statistical physics is that, for a homogeneous and isotropic system, the low-density limit of the radial pair distribution function, $g(r)$, is equal to the Boltzmann factor of the pair potential²⁸

$$\lim_{\rho \rightarrow 0} g(r) = \exp[-\beta U(r)]. \quad (10)$$

Ignoring the fact that Eq. (10) is strictly valid only for $\rho \rightarrow 0$, one can invert this relation to determine an expression for the PMF

$$U_0(r) := -k_B T \ln [g(r)]. \quad (11)$$

Note, that we replaced $U(r)$ with $U_0(r)$ in Eq. (11), as the resulting potential $U_0(r)$ is *not* necessarily the same as $U(r)$ anymore when $\rho > 0$. (More precisely, $U_0(r)$ is a free energy and not a potential energy, except for the special case $\rho = 0$.) This procedure for computing an approximative PMF is often referred to as Boltzmann Inversion (BI), and it can be refined using techniques like RMC¹⁶ or IBI¹⁹. These methods consist of alternating simulation and optimization steps, where the PMF is iteratively optimized until it reproduces the target radial pair distribution function, $\hat{g}(r)$, with sufficient accuracy (in what follows, we will mark all target quantities with a “hat” (^) symbol).

In RMC, an adjustment of the potential is accepted with a probability of

$$p = \min [1, \exp(-\Delta\chi_i^2/2)] \quad (12)$$

where the measure for the agreement between target and calculated $g_i(r)$ of the i -th iteration, χ_i^2 , is given by

$$\chi_i^2 = \sum [\hat{g}(r) - g_i(r)]^2 / \alpha^2 \quad (13)$$

where the parameter α adjusts the sensitivity of χ_i^2 to deviations in the radial distribution functions.

In IBI, an adjustment of the potential is done via

$$U_{i+1}(r) = U_i(r) - k_B T \ln \left[\frac{g_i(r)}{\hat{g}(r)} \right] \quad (14)$$

As a starting point, one typically uses $U_0(r)$ from Eq. (11).

In principle, such inversion schemes work rather well and they have been employed successfully for developing effective pairwise potentials from experimental structure measurements^{29–31} and for coarse-graining atomistic simulations.^{19,32–34} However, these methods are not guaranteed to yield physically accurate potentials as they are purely structure-based. The resulting PMF almost always exhibits a distinct state dependency,³⁵ which makes it difficult to transfer them from one state point to another. Further, although the IBI scheme should in principle provide a unique PMF for a given $\hat{g}(r)$,³⁶ in practice however, the convergence of Eq. (14) is difficult to achieve and varies in different parts of the PMF. Finally, both RMC and IBI require costly simulations for iteratively optimizing the PMF.

In this work we address these issues by employing NNs to determine a mapping between $g(r)$ and the PMF. Such a mapping could significantly speed up the process of finding the sought-after PMF by providing a better starting point for RMC or IBI, if not already returning the desired PMF itself. Furthermore, we hypothesize that providing additional physical information to the NN during the training phase will improve the transferability and representability of the predicted PMF.

B. Generation of data

In order to generate training data for the ML algorithms, a set of pair potentials $U(r)$ was constructed and the corresponding radial pair distribution functions $g(r)$ were generated from MD simulations in the canonical ensemble. If not stated otherwise explicitly, the particle diameter σ and the thermal energy $k_B T$ are used as the units of length and energy, respectively.

Pair potentials $U(r)$ are generated by first picking the cutoff distance $r_{\text{cut}} \in [0, 5]$ and the number of base points $n \in [6, 10]$, distributed randomly at distances in the range $[0, r_{\text{cut}}]$ with magnitudes in the interval $[0, 15]$. Then a smoothing spline function is applied to connect these points. Here, the degree of the spline function is randomly drawn between $k = 2$ and $k = 5$ to allow for a large variety of shapes (note that $k \geq 2$ is required to ensure differentiability of $U(r)$). To ensure physically meaningful pair potentials, the splines are fitted to the data with the constraint that the force $F(r) = -\nabla U(r)$ is continuous at the cutoff radius, *i.e.* $F(r_{\text{cut}}) = 0$. Further, the potentials are shifted so that $U(r_{\text{cut}}) = 0$. For the discretization of the generated potentials we chose 200 points that were evenly distributed in the interval $[0, r_{\text{cut}}]$. Using this procedure, 400 potentials were generated, where 100 of them had an additional hard-core contribution with diameter σ , modeled *via* the Weeks-Chandler-Andersen (WCA) potential.³⁷ Figure 1(a) shows a selection of potentials which have been generated using this procedure and have been employed in this work.

The MD simulations were conducted in a cubic simulation box with edge length $L = 40$ and periodic boundary conditions in all directions. The temperature was fixed at $T = 1$ using a Langevin thermostat with friction coefficient $\gamma = 1.0$ (note that the structural equilibrium properties of the system are independent of the specific γ value). The equations of motions were solved using the standard Velocity-Verlet algorithm with a time step of $\Delta t = 0.005\tau_{\text{MD}}$, where $\tau_{\text{MD}} = \sqrt{m\sigma^2/(k_B T)}$ is the intrinsic MD unit of time. In order to assess the density dependence of the pair potentials, simulations were conducted at four different number densities, *i.e.* $\rho = 0.125$ ($N = 8000$), $\rho = 0.244$ ($N = 15625$), $\rho = 0.512$ ($N = 32768$), and $\rho = 1.0$ ($N = 64000$). First, each simulation was run for 5×10^6 MD steps for equilibration (checked by monitoring the total potential energy of the system). Then, the systems were simulated for additional 5×10^6 MD steps to sample $g(r)$ (see Fig. 1(b,c) for examples). For the discretization of the calculated $g(r)$ we chose 200 points that were evenly distributed in the interval $[0, 20]$. In total, 770 simulations were conducted. Some simulations were discarded from our analysis, as they did not reach equilibrium in the allotted time, leading to a final number of 600 data sets. All simulations were performed using the HOOMD-blue software package.^{38,39}

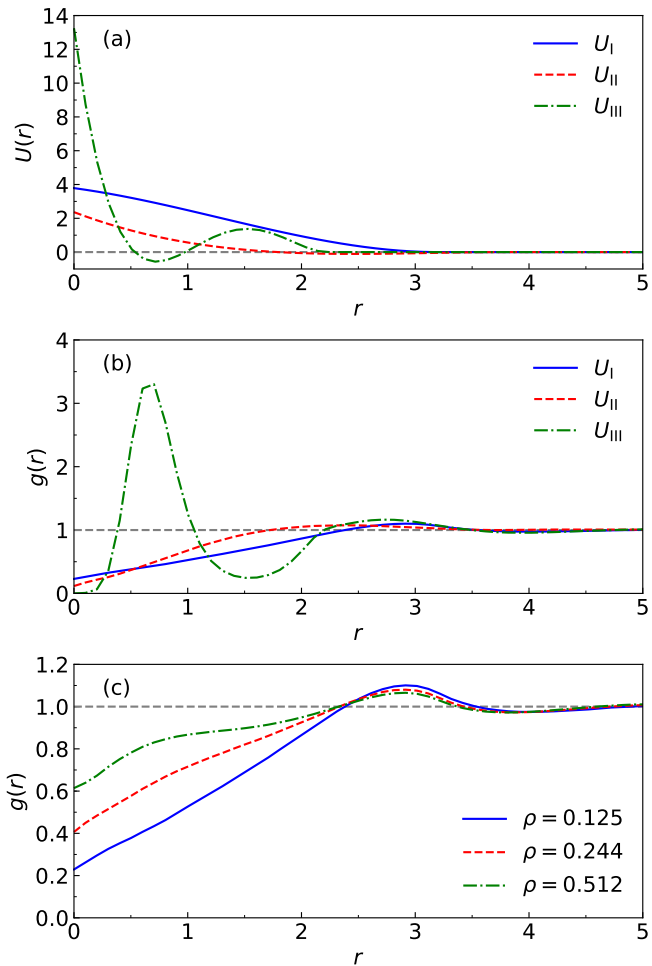


Figure 1. (a) Three selected pair potentials $U(r)$ used in this work, and (b) corresponding radial pair distribution functions, $g(r)$, recorded at number density $\rho = 0.125$. (c) $g(r)$ for U_I at three investigated values of ρ , as indicated.

C. Neural networks

1. Architecture and parameters

We used three different NN architectures in this work, *i.e.* a fully connected dense NN (DN), a convolutional NN (CN), and a U-Net⁴⁰ (UN). The DN consists of layers of neurons, where all neurons between two subsequent layers are connected to each other. Operations in the DN are limited to simple matrix-matrix and matrix-vector-multiplications, combined with activation functions to break the linearity. In contrast, the CN makes use of convolutional operations, where the number of parameters necessary to consider all possible correlations between points is drastically reduced compared to a DN. It is therefore useful to employ CNs for strongly correlated data, as it is typically the case in image processing but also in our problem. A special type of NNs that includes convolutional operations is the U-Net, which is based on

the so-called fully CN.⁴¹ In UNs, the input is first processed using convolutional layers then upsampled again and concatenated to a former stage of the processing, hence extracting features and combining these with the original input for further processing. This network architecture renders UNs especially useful for segmentation tasks.

One key aspect of our NNs is the loss function, which essentially controls the properties that should be optimized by the NN. We investigated in detail the influence of the chosen loss function and provide a more detailed discussion in Section II C 2. Further, the performance of an NN significantly depends on which information is provided to it, *e.g.* the global particle number density or the force. Also, the format in which this information is represented plays an important role. For instance, one could use $\exp[-\beta U(r)]$ rather than $U(r)$, since in this representation the absolute differences between different potentials is decreased, which may be favorable in cases with a strong repulsion combined with an attraction of significantly smaller strength. In Section III we study in detail the influence of these various aspects on the performance of the NNs.

In what follows, we will use the following naming convention to distinguish the NNs: For a given architecture X and given modifications y, we name the network X/y, *e.g.* for a UN with density information we use UN/d. The abbreviations for the different combinations of information can be found in Table I. Figure 2 shows schematic representations of the NNs used in this work.

| abbrev. | density | force | $\exp(-\beta U(r))$ |
|---------|---------|-------|---------------------|
| dfe | ✓ | ✓ | ✓ |
| fe | ✗ | ✓ | ✓ |
| de | ✓ | ✗ | ✓ |
| e | ✗ | ✗ | ✓ |
| df | ✓ | ✓ | ✗ |
| f | ✗ | ✓ | ✗ |
| d | ✓ | ✗ | ✗ |
| x | ✗ | ✗ | ✗ |

Table I. List of abbreviations for the additional informations provided to the networks.

An important issue in the implementation of the NNs is the treatment of hard-core potentials during the training process. For sufficiently strong repulsion, a further increase of the potential barrier does not change the physical properties of the potential. To this end, we first identify the distance r_{HC} where $U(r) \geq 20$. Then, we extend the hard-core potentials within $r < r_{\text{HC}}$ according to the function $U(r < r_{\text{HC}}) = k(r_{\text{HC}} - r)^{1.5} + U(r_{\text{HC}})$. Here, we matched the spring constant k , so that the original slope at the distance r_{HC} is recovered. The exponent of 1.5 is chosen to keep the overall range of the potential limited.

As activation functions used in our NNs, we chose between the scaled exponential linear unit (SELU), the parametric rectified linear unit (PReLU), the tangens hyperbolicus (tanh) and a linear activation function. For

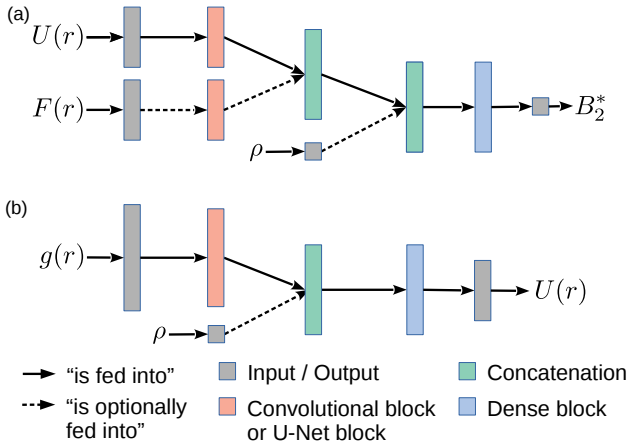


Figure 2. Schematic representation of (a) the CN used for computing the effective second virial coefficient, B_2^* (see Sec. III A), and (b) the UN used for computing the PMF (see Sec. III B).

the training, we employed an ADAM optimizer⁴² with a learning rate of 0.001. For the grid search, all NNs were trained for 10^4 epochs, while the final networks were trained for 2×10^5 epochs. All NNs have been constructed and trained using Tensorflow.⁴³ In order to find a suitable NN topology, an extensive grid search was conducted for all network architectures mentioned before. In this search, the influence of the loss function as well as the number and shape, *i.e.* width or number of filters and kernel size, of layers was studied. During this grid search, the aforementioned additional information was not provided to the networks. For each architecture, one network was chosen for further analysis.

2. Choosing appropriate loss functions

The loss functions used in the scope of this work were combinations of the three basic loss functions, the squared error (SE), the absolute error (AE), and the log-cosh error (LE). For a given pair of target and prediction, (\hat{y}, y) , the basic loss are

$$l_{\text{SE}}(\hat{y}, y) = (\hat{y} - y)^2 \quad (15)$$

$$l_{\text{AE}}(\hat{y}, y) = |\hat{y} - y| \quad (16)$$

$$l_{\text{LE}}(\hat{y}, y) = \ln [\cosh(\hat{y} - y)] \quad (17)$$

The loss of the entire output vector is then determined as the mean over the losses of the individual nodes. For instance, the mean squared error (MSE) is then given by

$$L_{\text{MSE}}(\hat{\mathbf{y}}, \mathbf{y}) = \frac{1}{d} \sum_{i=1}^d l_{\text{SE}}(\hat{y}_i, y_i) \quad (18)$$

with $\hat{\mathbf{y}}, \mathbf{y} \in \mathbb{R}^d$, where d denotes the dimensionality of the output vector (*e.g.* $d = 50$ for predicting pair potentials). Analogous expressions are used for L_{MAE} and

L_{MLE} . We indicate the average loss taken over multiple output vectors through angular brackets, $\langle \dots \rangle$.

For the NNs employed for finding the PMF from $g(r)$ data, one may of course use MD simulations to determine the $g(r)$ resulting from the predicted potential and compare its MSE with respect to the reference data (see Eq. (13)). However, this approach is prohibitively time consuming as it would require costly MD simulations at each step of the optimization procedure. Thus, the difference between $g(r)$ and $\hat{g}(r)$ is not a viable input for the loss function for training the NN, but can only be used as a final benchmark for the performance in selected instances. Instead, we directly compare the predicted pair potential, $U(r)$, with the target one, $\hat{U}(r)$. Such a comparison can be done with little cost and should reproduce the target potential by construction. It is, however, difficult to define a physically unique and meaningful measure of the difference between two pair potentials. The influence of different regions of the pair potential towards the pair distribution function are interlinked in a complex way, making it difficult to spatially separate and learn those effects independently. Therefore, it is essential to not only take into account the difference between single points of $U(r)$ and $\hat{U}(r)$, but also to consider the correlations between neighboring points. To take these long-distance correlations into account, we include additional terms in the loss function used for training NNs. These comprise of a Laplace-like term as well as loss terms correlating the differences of the potential at different distances

$$L_U = L_{\text{MLE}} + 0.8L_{\Delta} + \sum_{k=1}^5 L_k 0.8^k \quad (19)$$

Note that the weight of L_{Δ} and of each subsequent term of L_k is reduced by a factor of 0.8 to reduce their contribution with increasing distance.

The term L_{Δ} is the discretized Laplace term, which in the case of MSE reads

$$L_{\Delta} = \frac{1}{d-2} \sum_{i=1}^{d-2} l_{\text{SE}}(\hat{y}_{i+2} - 2\hat{y}_{i+1} + \hat{y}_i, y_{i+2} - 2y_{i+1} + y_i). \quad (20)$$

The loss terms L_k in Eq. (19) are given by the loss function applied to the difference of potential values being k indices apart. In the case of MSE this reads

$$L_k = \frac{1}{d-k} \sum_{i=1}^{d-k} l_{\text{SE}}(\hat{y}_{i+k} - \hat{y}_i, y_{i+k} - y_i) \quad (21)$$

To see how this definition of loss naturally introduces spatial correlations, one can rewrite L_k from Eq. (21) as follows

$$L_k = \frac{1}{d-k} \sum_{i=1}^{d-k} [l_{\text{SE}}(\hat{y}_{i+k}, y_{i+k}) + l_{\text{SE}}(\hat{y}_i, y_i) - 2(\hat{y}_{i+k} - y_{i+k})(\hat{y}_i - y_i)] \quad (22)$$

In this representation of L_k , it is clear that the last term in Eq. (22) introduces correlations between values at different distances.

3. Training performance

Finally, we checked if we have generated a sufficient amount of data for training our NNs. To this end, we trained one selected network architecture (UN/df) on subsets of the full training data, and compare $\langle L_{MLE} \rangle$ between the predicted and target potentials from the test set. For a given fraction f_{train} of the full training set, we use a random subset of the full training data, and carry out five independent runs for each fraction. To maintain the same diversity as the full training set, we ensure that the B_2 distribution of the subset is similar to that of the whole set. The results of this procedure are plotted in Fig. 3. We see that the loss reduces significantly from $\langle L_{MLE} \rangle \approx 0.15$ to $\langle L_{MLE} \rangle \approx 0.08$ as we increase f_{train} from 25% to 87%. The loss slightly increases again when the entire training data is utilized ($f_{\text{train}} = 100\%$), but this deviation is within the statistical uncertainties of our data.

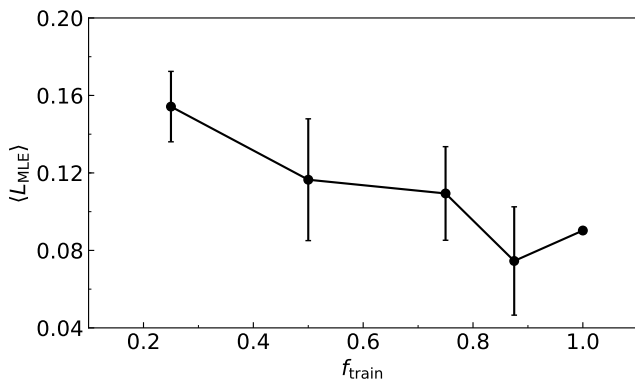


Figure 3. The mean logcosh loss, $\langle L_{MLE} \rangle$ between the predicted potentials from the testing data, $U(r)$, and the target potentials, $\hat{U}(r)$, as a function of f_{train} , the fraction of original training data being used for training the NN.

III. RESULTS

A. Predicting the equation of state

The aim of this section is to use NNs to learn a mapping from the pair potential, $U(r)$, to an effective second virial coefficient, B_2^* (see Section II A for details). Every selected NN was trained for all combinations of additional information using a four-fold cross-validation. The density, when provided, was included by merging it as a single additional input after convolutional operations. The force was included by applying the NN architecture

to both the potential as well as the force, and concatenating the outputs for further processing in fully dense layers. This procedure effectively doubles the size of the NN (see Fig. 2). As discussed in Section II, the input could additionally be modified by providing the potential in exponential space.

In Fig. 4, we plotted $\langle L_{MSE} \rangle$ and $\langle L_{MAE} \rangle$ between predicted and target pressures for the different architectures for different inputs. The errorbars in Fig. 4 were calculated as the standard error of the mean over all four folds. For comparison, the values obtained when using the analytical approximation of B_2 in Eq. (6) were $\langle L_{MSE} \rangle \approx 11.3$ and $\langle L_{MAE} \rangle \approx 1.1$, respectively. From these values, one can see that the NNs provide significantly more accurate predictions, even without providing any additional information to the NN. This behavior can be explained by the fact that the analytic expression for B_2 in Eq. (6) has been derived in the low-density limit and considers only two-body correlations. In contrast, the NN also incorporates higher correlations in B_2^* . From Fig. (4) it is apparent that the qualitative behavior of the different NN architectures for the different inputs is very similar, which is why it will be discussed solely for the case of the UN.

As one can see, the biggest improvement is achieved when including the density in the input. By providing the density, one essentially empowers the NN to learn the whole virial expansion in form of an effective second virial coefficient $B_2^*(\rho)$ rather than predicting a constant coefficient B_2^* with $dB_2^*/d\rho = 0$. In principle, it is possible to extract from this $B_2^*(\rho)$ the higher order virial coefficients B_i , by fitting $B_2^*(\rho)$ to a power series in ρ (see Eq. (2)).

Furthermore, one observes that using exclusively the force as additional input or providing the potential in exponential space does not alter the performance as significantly as the addition of the density. Combinations containing the density can improve the results even further. When including the force, however, one has to beware of overfitting due to the additional complexity that is introduced in the network. This behavior can be seen for example from the results for UN/dfe in Fig. 4, where the NN performs very good on the training set but significantly worse on the validation set, indicating that the NN is unable to generalize its observations. Again, the same trends could be observed for all topologies examined during this work.

The above mentioned observations and explanations are further confirmed when looking at Fig. 5, where the predicted pressures from the NNs for CN/x and CN/d are compared to the values extracted from the simulations. For comparability, all values were obtained for the same split of training and validation data. As one can see, there are some outliers for CN/x, which do not occur for CN/d, with the corresponding values stemming from the few simulations at high density ($\rho = 1.0$). By consulting Eq. (2), we conclude that these outliers are likely due to the fact that for increasing values of the

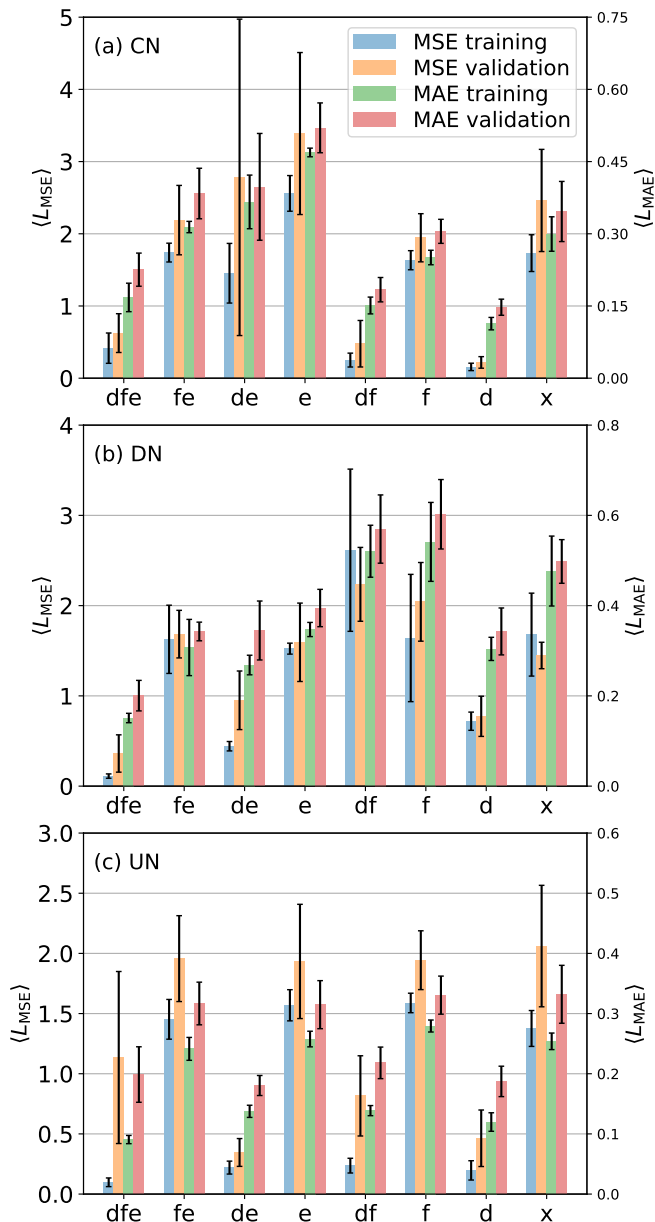


Figure 4. Comparison of $\langle L_{\text{MSE}} \rangle$ (left axis) and $\langle L_{\text{MAE}} \rangle$ (right axis) between predicted pressures, P , and target pressures, \hat{P} , for different NN topologies and inputs.

density, the higher order virial coefficients become more and more important, which cannot be accounted for in a non-density-dependent, constant B_2^* .

For the final topology we chose a CN with the density and the force as additional inputs, CN/df. This NN consists of a convolutional part containing two convolutional layers, with each layer having 32 filters with a kernel size of 5. In each layer, a batch normalization with a momentum of $m = 0.9$ was applied, followed by the convolution using a “same” padding and a SELU activation function. After the convolution, a max-pooling with a pool-size of $p = 2$ and a “same” padding was applied.

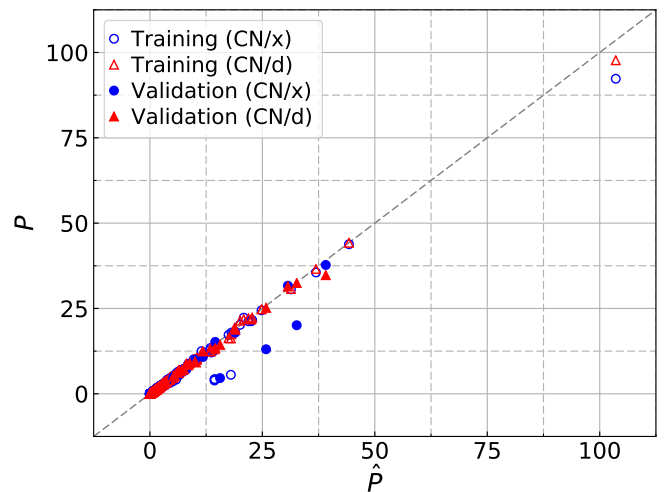


Figure 5. Comparison of the predicted pressure, P , vs. the target pressure, \hat{P} , using CN/x and CN/d.

This convolutional part is applied independently on both the potential and the force, which are passed to the NN. The outputs of this convolutional part are then flattened as well as concatenated together with the density information. Finally, a DN is applied to the output coming from the concatenation. This DN-part consisted of two dense layers with 128 and 64 neurons with a selu activation function and a dropout rate of 0.1, followed by a final output layer with one neuron and a linear activation function. The loss function that was used for this NN was L_{MLE} . Figure 2(a) shows a schematic representation of this NN.

For the training, all data (except those in the test set) were used. The corresponding results can be found in Fig. 6. Data from the training set are shown as open symbols, while those from the test set are shown with filled symbols. It is clear, that the predicted pressures from the CN/df outperform by far the estimates from the analytical expression in Eq. (7). This is especially true for those points calculated at high densities, where the low-density limit assumption breaks down. In contrast, all points predicted by the NN lie within a reasonable distance to the ground truth.

B. Potential prediction from pair distribution function

In order to use NNs for predicting the PMF from structural data, there are a few important issues to be tackled. For example, we have a choice regarding the input to the NN. Instead of directly feeding in the radial pair distribution function, $g(r)$, one could also use the approximation $U_0(r)$ from Eq. (11) as a starting point. The idea behind this approach is that $U_0(r)$ could serve as a good initial guess towards obtaining the target potential. To understand the effect of using $g(r)$ vs. $U_0(r)$ as an input to the NN, we take a UN including both density and force

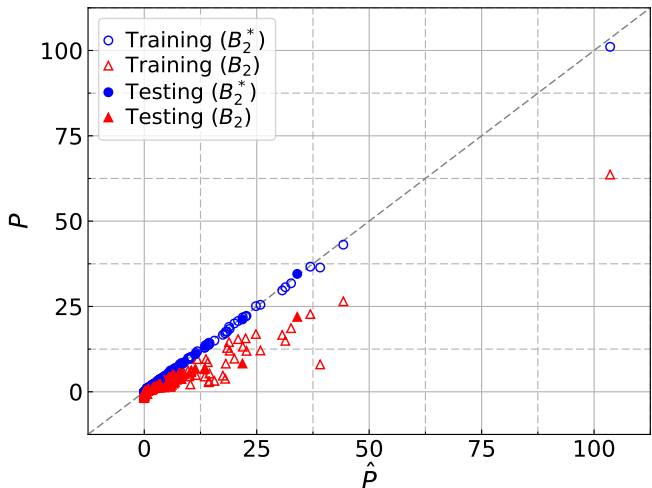


Figure 6. Predicted pressure, P , from CN/df (circles) and P estimated from Eq. (7) (triangles) vs. the target pressure, \hat{P} . Open and filled symbols show results from the training and testing set, respectively.

information. We denote the two varieties of the neural networks as UN/g and UN/BI, corresponding to the inputs $g(r)$ and $U_0(r)$, respectively.

To compare these two strategies, we compare the losses on the validation data set. The average loss across the validation set is about $\langle L_{\text{MLE}} \rangle \approx 0.040$ for UN/g, and $\langle L_{\text{MLE}} \rangle \approx 0.027$ for UN/BI. As a reference, the loss from simple BI is about $\langle L_{\text{MLE}} \rangle \approx 0.33$, *i.e.* about one order of magnitude higher than the results from the NNs. Figure 7 shows the probability distribution of the losses, which indicates that both average loss and the number of outliers are reduced when U_0 is used as the input of the NN instead of the raw pair distribution, $g(r)$. Because of this improved accuracy, we used $U_0(r)$ as the input for our NNs.

To determine which additional information (*e.g.* density, force) can improve the prediction of the PMF, we performed a grid search. We performed a four-fold cross-validation on each of the NN topologies studied. As a similarity metric for the predicted PMF, we use the error in the analytic estimate of B_2 (Eq. (6)) between the predicted and target potentials. This metric qualitatively estimates how close the physical behavior of the predicted potential is to that of the ground truth. In Fig. 8, we have plotted a comparison of the deviations between the analytic estimate of B_2 , computed using the predicted PMF, $U(r)$, and the target potentials, $\tilde{U}(r)$, for a few representative NN architectures. We observed that, in general, DNs performed significantly worse than UNs or CNs. This behavior is somewhat expected since DNs typically flatten the output, whereas spatial correlations in the pair potential values are best learned in NN architectures that take these correlations into account during the learning process (like CNs or UNs). Furthermore, we observed that including additional in-

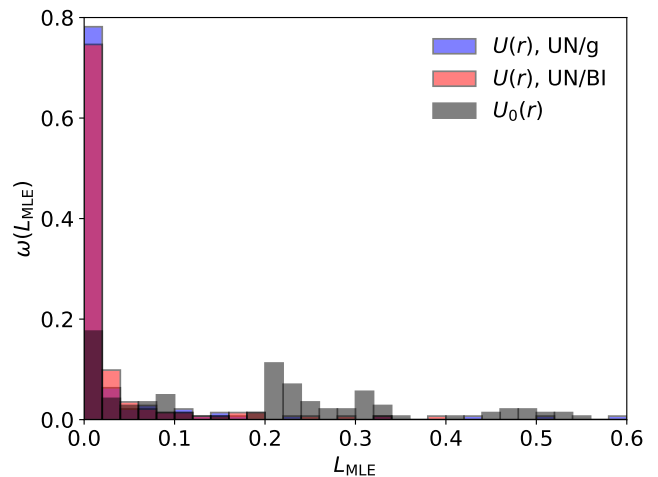


Figure 7. Probability distribution of losses of the UN/g and UN/BI networks for the validation data. For comparison, the loss from simple BI is also plotted.

formation on the density, and, more importantly, on the force, during the training process generally increased the accuracy of our predictions. In particular, UN/df and CN/f showed the best performance among all the network topologies tested.

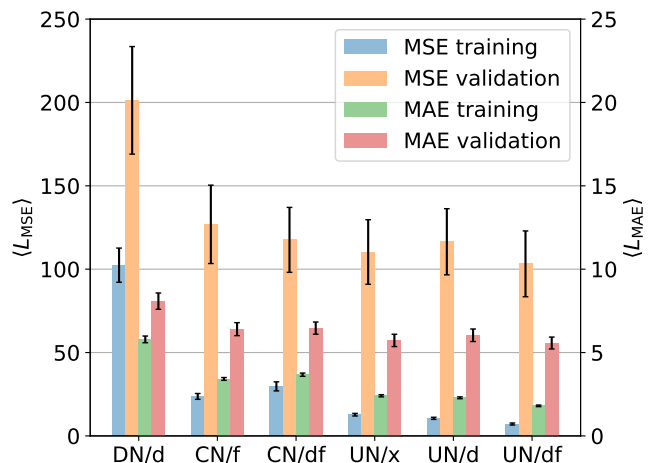


Figure 8. Comparison of $\langle L_{\text{MSE}} \rangle$ (left axis) and $\langle L_{\text{MAE}} \rangle$ (right axis) between the analytic estimate of B_2 using the predicted PMF, $U(r)$, and the target potentials, $\tilde{U}(r)$, for different NN architectures.

Comparison between different network topologies can also be done by directly comparing their prediction on a representative potential from the validation data. Such a comparison is shown in Fig. 9(a). We see that both UN/f and UN/df perform significantly better in terms of closer quantitative agreement, as well as similar qualitative trends with the ground truth. Importance of including the force in the training process can be traced back to the importance of spatial correlation information

that is conveyed through the forces; rather than trying to match the potential values at individual points, the network learns the spatial correlations and thus is able to extract physically more meaningful information. Including the force also teaches the NNs to avoid (unphysical) discontinuities in the predicted pair potentials. Further, we can see from the performance comparison of UN/d and UN/x in Fig. 8 that the addition of density alone in the input does not significantly improve the performance of the NN.

This discussion brings up the aspect of transferability of our predictions; given that $g(r)$ can vary significantly for the same potential at different densities, ρ , it is important to check whether the predicted PMF remains independent of ρ . Figure 9(b) shows a selected target potential from the validation set, $\hat{U}(r)$, and the corresponding predictions of $U(r)$ from the UN/df networks at different ρ . Indeed, the predicted potentials from the NN are quite close to the ground truth, and show only minor deviations at different ρ (as should be the case). In contrast, the PMF from simple BI, $U_0(r)$, provides a passable approximation of $\hat{U}(r)$ only at low densities, and the agreement gets significantly worse as the density increases.

As the final step, we chose the UN/df network, and trained it with all the data except those in the test set, using the loss given in Eq. (19). The predicted potentials are then used to compute B_2 using Eq. (6), and the resulting values are plotted against their target value, \hat{B}_2 , in Fig. 10(a). From this comparison it is clear, that B_2 and \hat{B}_2 closely match for the training data, providing a sanity check of our approach. The agreement is slightly worse for the testing data, but the prediction of the NN is still rather accurate. The deviations between B_2 and \hat{B}_2 are shown in more detail in Fig. 10(b), where we have plotted the probability distribution ω of the relative MAE between these two quantities, *i.e.* $|\hat{B}_2 - B_2|/\hat{B}_2$. Roughly one third of the predictions deviates by less than 5% from the ground truth, and only a small fraction of predictions show deviations of more than 50%.

To check if the predicted PMF from the UN/df network leads to a similar pair distribution function $g(r)$ as the original one, $\hat{g}(r)$, we ran MD simulations for selected cases from the test set, using the predicted potentials and calculated $g(r)$ for the resulting configurations. To compare the performance of the NN with simple BI, we also ran MD simulations with $U_0(r)$ and calculated the corresponding $g(r)$. Figure 11 shows the comparison of $g(r)$, where we have also included the employed pair potentials as insets of the corresponding plots. From these data, we can see that the PMF predicted from the NN, $U(r)$, reproduces $g(r)$ quite accurately in all cases shown here. Interestingly, the results for $g(r)$ obtained from using $U_0(r)$ are quite close to the target data, $\hat{g}(r)$, as well; only for the case shown in Fig. 11(d) we can see very strong deviations from the original $\hat{g}(r)$ in the region $r \lesssim 1$, which likely originate from the high particle density in this case. These trends are also reflected in the

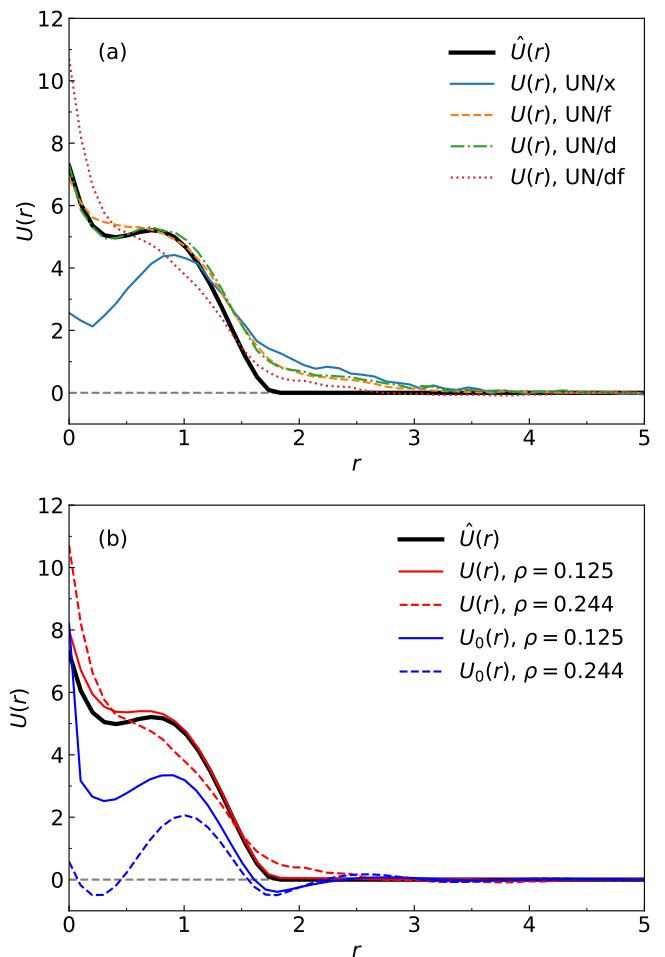


Figure 9. (a) Comparison of predicted PMF, $U(r)$, for different NNs, namely UN/x, UN/f, UN/d, and UN/df with the ground truth, $\hat{U}(r)$. (b) Comparison of potentials $U(r)$ generated by the UN/df and U_0 from simple BI, at densities $\rho = 0.125$ and $\rho = 0.244$. The ground truth, $\hat{U}(r)$, is also shown for comparison.

values of L_{MSE} between the original $\hat{g}(r)$ and the $g(r)$ computed from MD simulations with $U(r)$ and $U_0(r)$, respectively (given in the caption of Fig. 11).

To test the representability of the predicted potentials, *i.e.* how well they can reproduce physical quantities other than the radial distribution function, we analyzed the resulting pressures, P , and potential energies per particle, E/N . Figure 12(a) shows P obtained from the MD simulations conducted with $U(r)$ from the UN/df network and with $U_0(r)$ from simple BI *vs.* the pressure, \hat{P} , from the original MD simulations. For both cases, the agreement between P and \hat{P} is rather good at low pressures (and hence low densities), but it deteriorates as \hat{P} increases. In this higher pressure region, the results obtained with $U(r)$ from the UN/df network show similar qualitative trends as the target data, whereas the results obtained with $U_0(r)$ are too low and even become negative in one

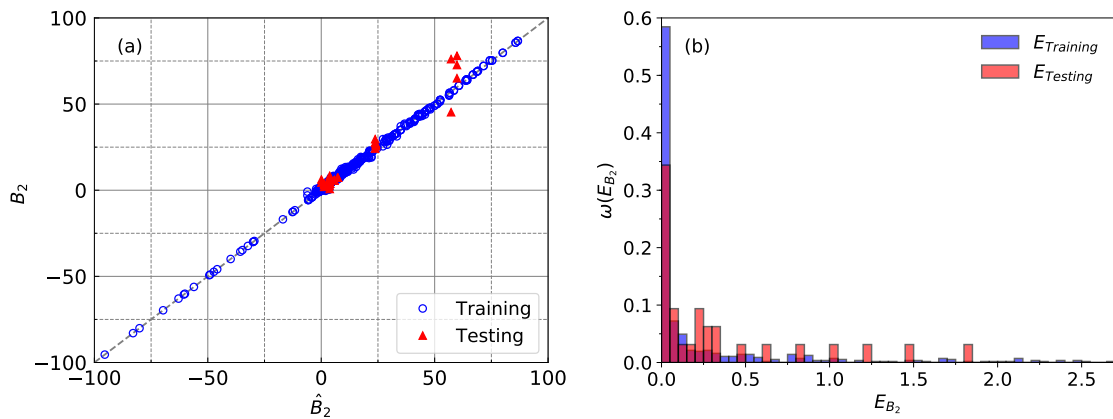


Figure 10. (a) Comparison of B_2 values from the predicted potentials from the UN/df network with the \hat{B}_2 values from the original potentials in the training and testing data. (b) Probability distribution ω of the relative error $|\hat{B}_2 - B_2|/\hat{B}_2$ from training and testing data.

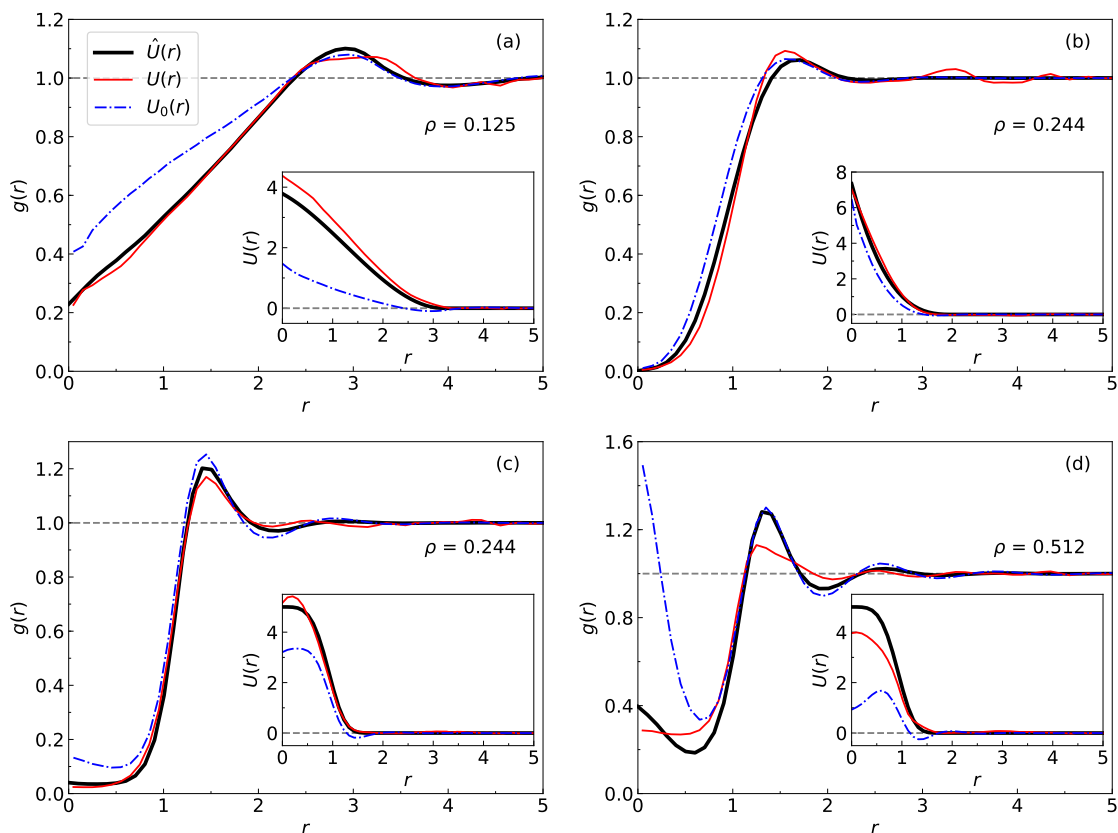


Figure 11. Comparison between original $\hat{g}(r)$ and $g(r)$ computed from MD simulations performed with $\hat{U}(r)$, $U(r)$ and $U_0(r)$, respectively, for selected cases of the test set. The corresponding potentials have been plotted in the insets. The L_{MSE} between $\hat{g}(r)$ and $g(r)$ for these cases are (a) 5.3×10^{-5} (2.7×10^{-3}), (b) 1.6×10^{-4} (9.9×10^{-4}), (c) 4.2×10^{-4} (1.2×10^{-3}), and (d) 1.3×10^{-3} (1.5×10^{-2}). The numbers in parentheses indicate the error for the BI data.

instance. This behavior can be seen also in Fig. 12(b), where we have plotted the distribution of pressure differences, $\Delta P = P - \hat{P}$, for both cases.

Similar trends can be also observed for the case of E/N , shown in Fig. 13, where the results from simple BI

show significantly stronger deviations compared to the original MD runs. For example, the MAE was about $\langle L_{\text{MAE}} \rangle = 4.6$ for the NN, while we found $\langle L_{\text{MAE}} \rangle = 8.6$ for the simulations conducted with $U_0(r)$.

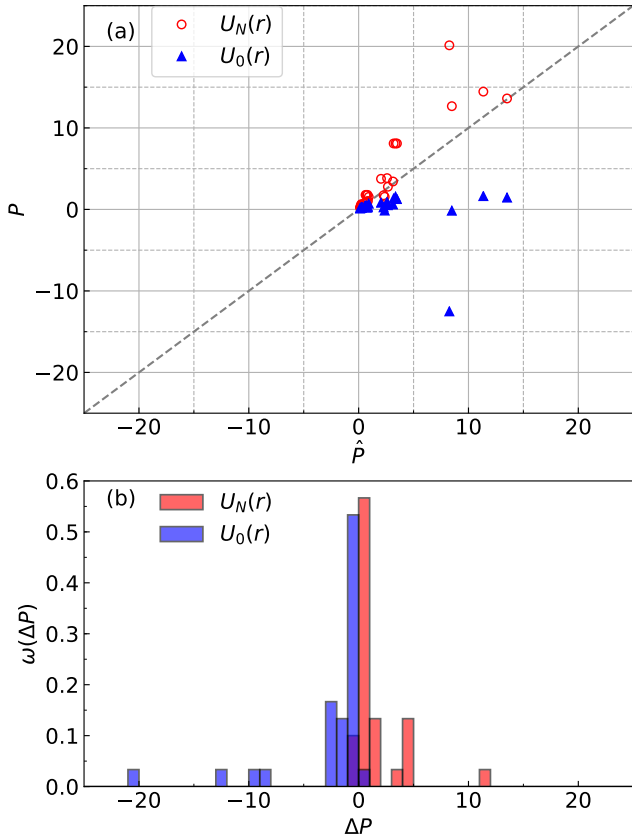


Figure 12. (a) Pressure, P , obtained from MD simulations using predicted potentials $U(r)$ (from UN/df) as a function of target pressure, \hat{P} . Results from simulations using $U_0(r)$ are shown also for comparison. (b) Distributions of pressure differences $\Delta P = P - \hat{P}$ from simulations conducted with $U(r)$ and $U_0(r)$.

IV. CONCLUSIONS

In this work we have developed strategies for using artificial neural networks (NNs) for predicting the equation of state (EOS) of soft materials, and for predicting the potential of mean force (PMF) from structural information based on the radial distribution function, $g(r)$. For both tasks, we investigated the influence of providing additional information, such as density and force, during the training procedure. For deriving the EOS task, we introduced an effective second virial coefficient, B_2^* , and found that the NNs provided a significantly more accurate description of the EOS compared to the virial expansion derived in the low-density limit. Further, we observed that providing density and force information improved the performance of the NNs, as this additional input allows the NNs to learn the whole virial expansion in form of an effective second virial coefficient $B_2^*(\rho)$. In future works, one could also determine the series of virial coefficients, B_i , using NNs by making the output of the NN multidimensional.

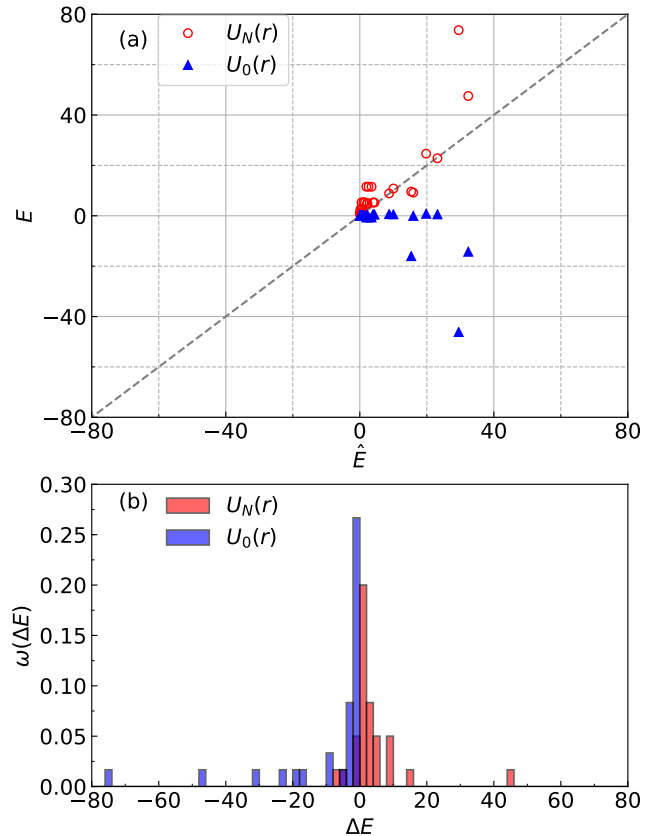


Figure 13. Same as Fig. 12, but for (a) potential energy per particle E/N , and (b) energy difference $\Delta E/N = (E - \hat{E})/N$.

Prediction of pair-potentials posed a significant challenge since assigning an objective and unique loss function for a potential vector during the training process is not a straight-forward task. In this work, we decided to compare directly the predicted potential, $U(r)$, with the target one, $\hat{U}(r)$, as opposed to comparing the resulting $g(r)$, in order to reduce the computational costs. We found that this approach leads to accurate predictions for both $U(r)$ and $g(r)$. We also saw that the addition of density and higher-order correlations of the potential (including the force) improved the performance of the NNs. We compared the results from the NNs with the ones obtained from simple Boltzmann inversion, *i.e.* $U_0(r) := -k_B T \ln[g(r)]$, and found that the NNs provided more accurate predictions for $U(r)$ and $g(r)$ in almost all investigated cases. Further, we investigated the representability of the predicted potentials, and found that the potentials from the NN reproduced the original data with much higher fidelity compared to $U_0(r)$.

There is, however, still room for future improvements: the PMF calculated from our NNs reproduce structural data with lower accuracy compared to potentials obtained from iterative methods, such as Iterative Boltzmann Inversion. Further, the training set used in this work only covers a subset of all conceivable cases. Nev-

ertheless, our NN approach is still a viable option for obtaining reasonably accurate initial estimates, which can then be optimized further using other methods until the desired accuracy is achieved. Such a combined approach could drastically cut down the computational cost and development time for coarse-graining applications, and it could also be a useful tool for inverse problems in materials discovery in soft matter.

ACKNOWLEDGEMENTS

This work was funded by the German Research Foundation (DFG) through project number 233630050 - TRR 146. MRK and AN further acknowledge financial support provided by the DFG through project number NI 1487/2-1. Computing time was granted on the supercomputer Mogon at Johannes Gutenberg University Mainz (www.hpc.uni-mainz.de).

REFERENCES

- ¹M. G. Noro and D. Frenkel, *J. Chem. Phys.* **113**, 2941 (2000).
- ²P. J. Lu, E. Zaccarelli, F. Ciulla, A. B. Schofield, F. Sciortino, and D. A. Weitz, *Nature* **453**, 499 (2008).
- ³P. Bolhuis, A. Louis, J. Hansen, and E. Meijer, *J. Chem. Phys.* **114**, 4296 (2001).
- ⁴C. N. Likos, *Physics Reports* **348**, 267 (2001).
- ⁵F. Sciortino, S. Mossa, E. Zaccarelli, and P. Tartaglia, *Phys. Rev. Lett.* **93**, 055701 (2004).
- ⁶S. Mossa, F. Sciortino, P. Tartaglia, and E. Zaccarelli, *Langmuir* **20**, 10756 (2004).
- ⁷B. M. Mladek, G. Kahl, and C. N. Likos, *Phys. Rev. Lett.* **100**, 028301 (2008).
- ⁸K. Ho, C. T. Chan, and C. M. Soukoulis, *Phys. Rev. Lett.* **65**, 3152 (1990).
- ⁹O. Sigmund and S. Torquato, *Applied Physics Letters* **69**, 3203 (1996).
- ¹⁰G. Férey and A. K. Cheetham, *Science* **283**, 1125 (1999).
- ¹¹H. M. Jaeger, *Soft matter* **11**, 12 (2015).
- ¹²B. A. Lindquist, R. B. Jadrich, and T. M. Truskett, *J. Chem. Phys.* **145**, 111101 (2016).
- ¹³D. Chen, G. Zhang, and S. Torquato, *J. Phys. Chem. B* **122**, 8462 (2018), pMID: 30088925.
- ¹⁴M. R. Khadilkar, S. Paradiso, K. T. Delaney, and G. H. Fredrickson, *Macromolecules* **50**, 6702 (2017).
- ¹⁵K. R. Gadelrab, A. F. Hannon, C. A. Ross, and A. Alexander-Katz, *Mol. Syst. Des. Eng.* **2**, 539 (2017).
- ¹⁶R. L. McGreevy and L. Pusztai, *Molecular Simulation* **1**, 359 (1988), <https://doi.org/10.1080/08927028808080958>.
- ¹⁷D. Keen and R. McGreevy, *Nature* **344**, 423 (1990).
- ¹⁸A. P. Lyubartsev and A. Laaksonen, *Phys. Rev. E* **52**, 3730 (1995).
- ¹⁹D. Reith, M. Ptz, and F. Müller-Plathe, *J. Comput. Chem.* **24**, 1624 (2003).
- ²⁰M. C. Rechtsman, F. H. Stillinger, and S. Torquato, *Phys. Rev. Lett.* **95**, 228301 (2005).
- ²¹M. S. Shell, *J. Chem. Phys.* **129**, 144108 (2008).
- ²²J. Behler, *J. Chem. Phys.* **145**, 170901 (2016).
- ²³D. J. Audus and J. J. de Pablo, *ACS Macro Lett.* **6**, 1078 (2017).
- ²⁴A. L. Ferguson, *J. Phys.: Condens. Matter* **30**, 043002 (2017).
- ²⁵T. Bereau, R. A. DiStasio Jr., A. Tkatchenko, and A. O. von Lilienfeld, *J. Chem. Phys.* **DETC2018**, 241706 (2018).
- ²⁶T. Bereau, “Data-driven methods in multiscale modeling of soft matter,” in *Handbook of Materials Modeling : Methods: Theory and Modeling*, edited by W. Andreoni and S. Yip (Springer International Publishing, Cham, 2018) pp. 1–12.
- ²⁷N. E. Jackson, M. A. Webb, and J. J. de Pablo, *Curr. Opin. Chem. Eng.* **23**, 106 (2019).
- ²⁸J.-P. Hansen and I. R. McDonald, *Theory of simple liquids*, 3rd ed. (Academic Press, 2006).
- ²⁹K. Reatto, D. Levesque, and J. J. Weiss, *Phys. Rev. A* **33**, 3451 (1986).
- ³⁰K. Müller, N. Osterman, Babič, C. N. Likos, J. Dobnikar, and A. Nikoubashman, *Langmuir* **30**, 5088 (2014).
- ³¹L. Song, L. Yang, J. Meng, and S. Yang, *J. Phys. Chem. Lett.* **8**, 347 (2017).
- ³²F. Müller-Plathe, *CHEMPHYSICHEM* **3**, 754 (2002).
- ³³G. Milano and F. Müller-Plathe, *J. Phys. Chem. B* **109**, 18609 (2005).
- ³⁴B. Bayramoglu and R. Faller, *Macromolecules* **45**, 9205 (2012).
- ³⁵A. A. Louis, *J. Phys.: Condens. Matter* **14**, 9187 (2002).
- ³⁶R. L. Henderson, *Phys. Lett. A* **49**, 197 (1974).
- ³⁷J. D. Weeks, D. Chandler, and H. C. Andersen, *J. Chem. Phys.* **54**, 5237 (1971).
- ³⁸J. A. Anderson, C. D. Lorenz, and A. Travesset, *J. Comput. Phys.* **227**, 5342 (2008).
- ³⁹J. Glaser, T. D. Nguyen, J. A. Anderson, P. Lui, F. Spiga, J. A. Millan, D. C. Morse, and S. C. Glotzer, *Comput. Phys. Commun.* **192**, 97 (2015).
- ⁴⁰O. Ronneberger, P. Fischer, and T. Brox, in *Medical Image Computing and Computer-Assisted Intervention – MICCAI 2015*, edited by N. Navab, J. Hornegger, W. M. Wells, and A. F. Frangi (Springer International Publishing, Cham, 2015) pp. 234–241.
- ⁴¹J. Long, E. Shelhamer, and T. Darrell, in *2015 IEEE Conference on Computer Vision and Pattern Recognition (CVPR)* (2015) pp. 3431–3440.
- ⁴²D. Kingma and J. Ba, *ICLR* (2014).
- ⁴³M. Abadi, A. Agarwal, P. Barham, E. Brevdo, Z. Chen, C. Citro, G. S. Corrado, A. Davis, J. Dean, M. Devin, S. Ghemawat, I. Goodfellow, A. Harp, G. Irving, M. Isard, Y. Jia, R. Jozefowicz, L. Kaiser, M. Kudlur, J. Levenberg, D. Mané, R. Monga, S. Moore, D. Murray, C. Olah, M. Schuster, J. Shlens, B. Steiner, I. Sutskever, K. Talwar, P. Tucker, V. Vanhoucke, V. Vasudevan, F. Viégas, O. Vinyals, P. Warden, M. Wattenberg, M. Wicke, Y. Yu, and X. Zheng, “TensorFlow: Large-scale machine learning on heterogeneous systems,” (2015), software available from tensorflow.org.